Journal of The Electrochemical Society

The Electrochemical Society
Advancing solid state & electrochemical science & technology

OPEN ACCESS

Orthotropic Viscoelastic Modeling of Polymeric Battery Separator

To cite this article: Shutian Yan *et al* 2020 *J. Electrochem. Soc.* **167** 090530

View the article online for updates and enhancements.



This content was downloaded from IP address 128.219.44.55 on 04/05/2020 at 15:20

Journal of The Electrochemical Society, 2020 **167** 090530

Orthotropic Viscoelastic Modeling of Polymeric Battery Separator

Shutian Yan,[1] Jie Deng,[2] Chulheung Bae,[2] Sergiy Kalnaus,[3] and Xinran Xiao[1,z]

[1]*Composite Vehicle Research Center, Department of Mechanical Engineering, Michigan State University, Lansing, Michigan 48910, United States of America*
[2]*Department of Energy Storage Research, Ford Motor Company, Dearborn, Michigan 48124, United States of America*
[3]*Computational Sciences and Engineering Division, Oak Ridge National Laboratory, Oak Ridge, Tennessee 37830, United States of America*

The separator is one of the most important components for battery safety since its failure can cause short-circuit that may lead to thermal runaway. As such, understanding the mechanical behaviors of separators is critical to improve battery safety. Nevertheless, modeling the mechanical behaviors of separators is challenging since they usually depend on multiple factors such as orientation, temperature and strain rate due to the microstructure of separators. Here we develop an orthotropic linear viscoelastic model for separators, which takes both anisotropy and strain rate effects into account. This model is the first step of a future model that considers more factors such as temperature and large deformation. The model has been implemented as a user material model in a finite element package, where a discretization algorithm is developed to evaluate the stiffness-based hereditary integral with a kernel of Prony series. The user model has been applied to a polypropylene (PP) separator Celgard® 2400. The simulation results agree well with experimental data, which include the rate dependent uniaxial tensile behavior of the separator in the two in-plane material directions and in shear, and the strain contour patterns of every strain component during biaxial tension.
© 2020 The Author(s). Published on behalf of The Electrochemical Society by IOP Publishing Limited. This is an open access article distributed under the terms of the Creative Commons Attribution 4.0 License (CC BY, http://creativecommons.org/licenses/by/4.0/), which permits unrestricted reuse of the work in any medium, provided the original work is properly cited. [DOI: 10.1149/1945-7111/ab8a99]

Manuscript submitted January 8, 2020; revised manuscript received March 18, 2020. Published April 29, 2020. *This paper is part of the JES Focus Issue on Battery Safety, Reliability and Mitigation.*

The separator is critical to battery safety since it separates positive and negative electrodes and its failure can directly cause short-circuit that may lead to a catastrophic consequence. Thus, to improve battery safety, it is important to understand the responses of separators under different scenarios such as impact and thermal ramp. Due to the microstructure of separators, their mechanical behaviors are very complex. For instance, depending on the manufacture process, a separator can exhibit significantly different behaviors in two in-plane directions. Moreover, since a separator is usually a porous polymer, its responses generally dependent on both strain rate and temperature. In addition, some separators may shrink considerably at elevated temperatures.[1,2] Since separators are fully constrained in batteries, a large shrinkage in a separator can induce high stress and failure. As such, to understand and model the thermomechanical behavior of separators, at least four important aspects of constitutive behaviors must be included: (1) material anisotropy; (2) rate dependency[3–8]; (3) temperature dependency[3–7]; and (4) thermal shrinkage.

So far, few works have modeled the separator in Finite Element Analysis (FEA) explicitly and none of them has considered all four aspects of the constitutive behaviors. For example, the separators in lithium ion batteries have been modeled as an isotropic viscoelastic material[9,10] which ignored the anisotropy; with an anisotropic honeycomb model which did not consider the time and temperature dependence[11]; and with an anisotropic viscoplastic Bergstrom-Boyce model[12] which did not consider the temperature dependence. In commercial finite element codes for crash safety simulations, e.g. LS-DYNA®, there is no suitable model to represent the orthotropic thermomechanical behavior of battery separators.

To address this need, an orthotropic thermomechanical model based on the time-temperature superposition principle of the viscoelasticity theory[13,14] is under development. To support this development, we have investigated the experimental techniques for the measurement of thermal expansion/shrinkage behavior[2] and orthotropic viscoelastic behavior[15] of the battery separators. This paper presents the model development. As the first step, an orthotropic linear viscoelastic model has been developed and implemented into the commercial FE package LS-DYNA® as a user defined material model. For this implementation, a discretization algorithm for the evaluation of a stiffness-based hereditary integral with a kernel of a single exponential function has been extended to a kernel of Prony series. The implemented model has been verified and validated for a polypropylene (PP) separator Celgard® 2400 with the experimental data obtained under uniaxial creep, uniaxial tension at different loading rates, and under biaxial loading with punch test.

Orthotropic Viscoelastic Model and Its Implementation in LS-DYNA®

The model developed in this work is aimed for crash simulations. LS-DYNA® is a common software used in such applications. As the user material model in LS-DYNA is stiffness based, the discussion will be focused on this formulation.

The stress-strain behavior of a linear viscoelastic material in terms of stiffness is described as[13,14]

$$\sigma(t) = \int_0^t G(t-t')\frac{d\varepsilon}{dt'}dt' \qquad [1]$$

where $G(t)$ is the relaxation stiffness matrix.

The components of the stiffness matrix are often expressed by Prony series

$$G_{ij}(t) = G_{ij}^{\infty} + \sum_{i=1}^{n} G_{ij}^{i}\exp(-t/\tau_i) \qquad [2]$$

where G^{∞} is the fully relaxed modulus, G^i is the relaxation constant, and τ_i is the characteristic relaxation time for the ith term, respectively.

Discretization algorithm of hereditary integral with a kernel of Prony series.—The main challenge in implementing the viscoelastic model into LS-DYNA® is the evaluation of the hereditary integral in Eq. 1. The stress relaxation depends on the time elapsed for the strain increment at each time step. For a process with an arbitrarily varying stress strain history, a direct evaluation of the hereditary integral would require storing the strain increment at each time step. This algorithm would be prohibitively expensive.

Puso and Weiss[16] presented an algorithm for the evaluation of hereditary integral with a single exponential function as its kernel.

[z]E-mail: xinran@egr.msu.edu

This starts from the analysis of Eq. 1. At time $t + \Delta t$, Eq. 1 becomes

$$\sigma(t+\Delta t) = \int_0^{t+\Delta t} G(t+\Delta t - t')\frac{d\epsilon}{dt'}dt' \quad [3]$$

Equation 3 can be separated into two terms

$$\sigma(t+\Delta t) = \int_0^{t} G(t+\Delta t - t')\frac{d\epsilon}{dt'}dt' + \int_t^{t+\Delta t} G(t+\Delta t - t')\frac{d\epsilon}{dt'}dt \quad [4]$$

where each term will be evaluated separately. The 2nd term on the right hand side of the Eq. 4 can be solved approximately by using the Mean Value Theorem when Δt is very small:

$$\int_t^{t+\Delta t} G(t+\Delta t - t')\frac{d\epsilon}{dt'}dt' = \frac{\varepsilon_{t+\Delta t} - \varepsilon_t}{\Delta t} \times \int_t^{t+\Delta t} G(t+\Delta t - t')dt' = \frac{\varepsilon_{t+\Delta t} - \varepsilon_t}{\Delta t} G(\Delta t)\Delta t \quad [5]$$

To evaluate the 1st term in Eq. 4, a specific kernel function has to be defined. Assuming $G(t)$ is a single term exponential function

$$G(t) = C_1 \exp\left(-\frac{t}{\tau}\right) \quad [6]$$

The 1st term becomes

$$\int_0^t G(t+\Delta t - t')\frac{d\varepsilon}{dt'}dt' = \int_0^t C_1 \exp\left(-\frac{t+\Delta t - t'}{\tau}\right)\frac{d\varepsilon}{dt'}dt' = \exp\left(-\frac{\Delta t}{\tau}\right)\int_0^t C_1 \exp\left(-\frac{t-t'}{\tau}\right)\frac{d\varepsilon}{dt'}dt' = \exp\left(-\frac{\Delta t}{\tau}\right)\sigma(t) \quad [7]$$

The significance of Eq. 7 is that, to evaluate the hereditary integral at $t + \Delta t$, we only need to know the stress at the previous time step. Based on this mathematical derivation, a discretization algorithm for the evaluation of hereditary integral with a kernel of a single exponential function has been developed.[16]

A single exponential function is insufficient to represent the relaxation stiffness over a broad time spectrum. To extend the algorithm to hereditary integral with a kernel of Prony series, we examine the generalized Maxwell model in Fig. 1, which is the physical representation of Eq. 2. It shows that the total stress in the material is contributed by the long-term relaxation stress σ_∞ and n individual Maxwell components, each with its characteristic relaxation time τ_i (i = 1, 2, ... n). If the stress in each Maxwell component is known, the total stress will be

$$\sigma(t) = \sigma_\infty + \sum_{i=1}^{n} \sigma^i(t) \quad [8]$$

Following the same mathematical operation as in Eq. 7, the 1st term of Eq. 4 is derived for a kernel of Prony series as

$$\int_0^t G(t+\Delta t - t')\frac{d\varepsilon}{dt'}dt = \sigma_\infty + \sum_{i=1}^{n}\exp\left(-\frac{\Delta t}{\tau_i}\right) \times \int_0^t G_i \exp\left(-\frac{t-t'}{\tau_i}\right)\frac{d\varepsilon}{dt'}dt' = \sigma_\infty + \sum_{i=1}^{n}\exp\left(-\frac{\Delta t}{\tau_i}\right)\sigma^i(t) \quad [9]$$

The evaluation of Eq. 9 requires the stress value in each Maxwell component in the previous step. As the Prony series contains a limited number of terms, the required storage can be easily managed.

Figure 2 presents the flowchart for the implementation of this algorithm in LS-DYNA. At step j, for a time increment of Δt, the stress increment $\Delta\sigma$ is contributed by the long-term relaxation stress $\Delta\sigma_\infty$ and the sum of individual Maxwell components

$$\Delta\sigma = \Delta\sigma_\infty + \sum_{i=1}^{n}\Delta\sigma^i \quad [10]$$

For the ith Maxwell component, the stress change $\Delta\sigma^i$ is composed of the stress increment at the current step, and the continuous relaxation of the stress accumulated up to the previous step

$$\Delta\sigma^i = G_i \exp\left(-\frac{\Delta t}{\tau_i}\right)\Delta e + \left[\exp\left(-\frac{\Delta t}{\tau_i}\right)\sigma^i(t) - \sigma^i(t)\right] \quad [11]$$

Next, the stress for individual Maxwell components and the total stress are updated and stored for use at the next time step.

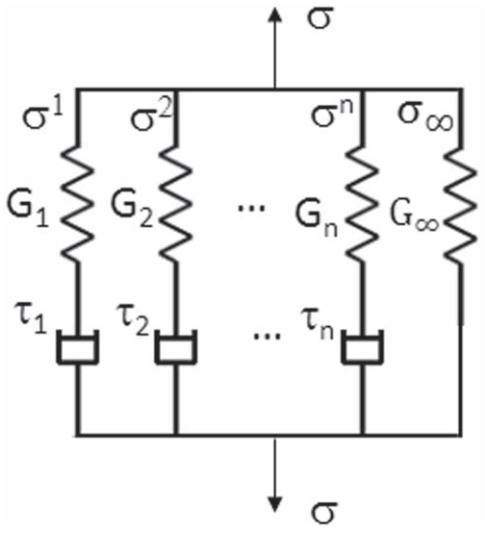

Figure 1. The generalized Maxwell model.

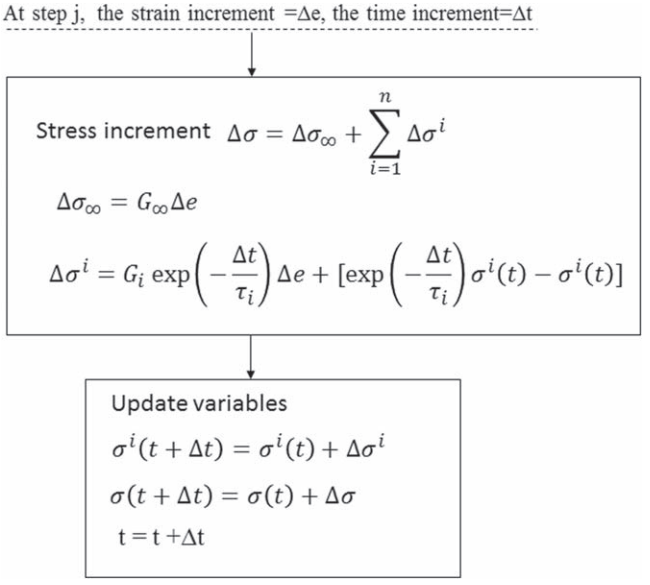

Figure 2. Flowchart for the implementation of evaluation of hereditary integral with Prony series.

Relaxation stiffness matrix for plane stress state.—Li et al., has presented an orthotropic viscoelastic model for polyethylene thin films.[17] The model was formulated in compliance based form for plane-stress condition. Similarly, the stiffness matrix under the plane stress condition for an orthotropic viscoelastic material is given by

$$[\boldsymbol{G}(t)] = \frac{1}{1-\nu_{12}\nu_{21}}\begin{bmatrix} G_{11}(t) & \nu_{12}G_{22}(t) & 0 \\ \nu_{12}G_{22}(t) & G_{22}(t) & 0 \\ 0 & 0 & (1-\nu_{12}\nu_{21})\,G_{66}(t) \end{bmatrix} \quad [12]$$

where $G_{11}(t)$ and $G_{22}(t)$ are the modulus in the 1st and 2nd material directions in-plane, $G_{66}(t)$ is the in-plane shear modulus, and ν_{12} and ν_{21} are the major and minor Poisson's ratios. Based on our experimental work on Celgard® 2400 separator,[15] in the linear viscoelastic range, the symmetry condition $\nu_{21} = \nu_{12} \times \frac{G_{22}(t)}{G_{11}(t)}$ is valid and ν_{12} is approximately a constant. In Eq. 12, therefore, there are four independent material properties $G_{11}(t)$, $G_{22}(t)$, $G_{66}(t)$, and ν_{12}. ν_{12} is assumed to be a constant.

For shell element, in the situation when out-of-plane bending is involved such as in punch test simulations, the out-of-plane shear stress is calculated as

$$\sigma_{23}(t) = \int_0^t G_{44}(t-t')\frac{d\gamma_{23}}{dt'}dt' \quad [13]$$

$$\sigma_{13}(t) = \int_0^t G_{55}(t-t')\frac{d\gamma_{13}}{dt'}dt' \quad [14]$$

In the current work, the material is assumed to be transversely isotropic and hence $G_{55}(t) = G_{66}(t)$, and $G_{44}(t) = \frac{G_2(t)}{2(1+\nu_{23})}$. Since it is difficult to measure the Poisson's ratio ν_{23}, a parameter study of ν_{23} as 0.1, 0.2, and 0.3 is carried out to examine the influence of ν_{23} on the prediction. It was found that the magnitude of ν_{23} does not have influence on the simulated strains at the upper surface in punch test simulations.

Experimental

The polymer separator investigated in this work was a commercial product Celgard® 2400. It is a monolayer PP porous film with a nominal thickness of 25 μm. This separator is dry processed. The two in-plane principal material directions are referred to as the machine direction (MD) and the transverse direction (TD).

The viscoelastic properties of Celgard® 2400 in the MD, TD, and shear directions have been characterized in our previous work.[15] In Ref. 15, the viscoelastic properties were measured at 28C and model parameters were valid up to 0.001/s strain rates. To cover higher strain rates, additional creep experiments have been performed at 22 °C and 14 °C. At a lower temperature, the viscoelastic relaxation was slower. In this way, the relaxation that occurs too quickly to be measured accurately in experiments conducted at higher temperatures can be captured in measurement at lower temperatures. Based on the time-temperature-superposition principle,[13,14] these data can be added to the master curve at 28 °C. Table I summarizes the Prony series parameters for the relaxation moduli of Celgard® 2400. These models are valid up to 10/s. Over the strain range of 0.1 to 5%, the measured major Poisson's ratio ν_{12} was nearly a constant, $\nu_{12} = 0.17$. The parameters in Table I and ν_{12} value are the required input for the orthotropic linear viscoelastic model.

To validate the model, a biaxial punch experiment has been performed in the current work. Figure 3 presents this experiment. The setup is similar to a dome test/the deep drawing test in sheet metal forming research. The current setup was developed specifically for testing battery separators.[18] The separator to be tested has a diameter 120 mm. For the digital image correlation (DIC) measurements, a speckle pattern was sprayed on the separator using the stencil ink. The separator was sandwiched between a pair of unthreaded polyvinyl chloride flanges. The edges of the inner flange opening were chamfered and smoothed (Fig. 3c); in addition, rubber gaskets were placed between the flanges and the sample to avoid any tearing of the separator. The flange had an opening of 33.8 mm diameter.

The flange assembly with gaskets and separator was clamped in a steel frame which was mounted on an MTS servo hydraulic load frame equipped with 200 N load cell. The clamping pressure was evenly distributed over the flanges by using four pairs of steel nuts. The deformation was imparted on the sample by moving a ball upward thus creating a biaxial stretch of the sample. The PTFE sphere with a diameter of 25.4 mm (US Plastic Corp) was used for this purpose. PTFE was chosen in order to minimize friction between separator and the ball. The sphere was seated on the cylindrical steel rod with concave surface as shown in Fig. 3b. It was not rigidly coupled to the load train of the equipment to avoid any bending or torsion. The speed of the ball was maintained at 0.2 mm s^{-1} in the experiments. All experiments were done at room temperature and in ambient air.

The setup was equipped with two charge-coupled device (CCD) cameras and a light emitting diode (LED) light source to capture the images during the sample loading as shown in Fig. 3e. The recording was performed by Vic3D software by Correlated Solutions. The recording frequency was 4 Hz. The two cameras were successfully calibrated using a small grid with 3 mm step size.

The actuator was moved to contact with the sample and this first image was used as the reference for displacement calculation. The strains were calculated using the vertical displacement component.

Table I. Prony series parameters for the relaxation moduli of Celgard® 2400.

Updated MD G_{11}(t)		Updated TD G_{22}(t)		Updated Shear G_{66}(t)	
Stress relaxation constant (N/m^2)	Relaxation time (s)	Stress relaxation constant (N/m^2)	Relaxation time (s)	Stress relaxation constant (N/m^2)	Relaxation time (s)
$G_\infty = 6.72 \times 10^8$	—	$G_\infty = 3.62 \times 10^8$	—	$G_\infty = 6.35 \times 10^7$	—
$G_1 = 2.74 \times 10^8$	$\tau_1 = 8.86 \times 10^{-4}$	$G_1 = 3.99 \times 10^7$	$\tau_1 = 9.40 \times 10^{-4}$	$G_1 = 1.48 \times 10^7$	$\tau_1 = 9.00 \times 10^{-4}$
$G_2 = 2.29 \times 10^8$	$\tau_2 = 8.92 \times 10^{-3}$	$G_2 = 3.93 \times 10^7$	$\tau_2 = 9.36 \times 10^{-3}$	$G_2 = 9.71 \times 10^6$	$\tau_2 = 9.27 \times 10^{-3}$
$G_3 = 3.63 \times 10^8$	$\tau_3 = 0.0806$	$G_3 = 3.50 \times 10^7$	$\tau_3 = 0.0939$	$G_3 = 1.06 \times 10^7$	$\tau_3 = 0.0914$
$G_4 = 1.41 \times 10^8$	$\tau_4 = 0.907$	$G_4 = 2.27 \times 10^7$	$\tau_4 = 0.958$	$G_4 = 7.77 \times 10^6$	$\tau_4 = 0.931$
$G_5 = 2.58 \times 10^8$	$\tau_5 = 8.13$	$G_5 = 4.17 \times 10^7$	$\tau_5 = 9.20$	$G_5 = 1.43 \times 10^7$	$\tau_5 = 8.65$
$G_6 = 1.94 \times 10^8$	$\tau_6 = 82.7$	$G_6 = 2.00 \times 10^7$	$\tau_6 = 95.9$	$G_6 = 1.38 \times 10^7$	$\tau_6 = 84.8$
$G_7 = 2.44 \times 10^8$	$\tau_7 = 728$	$G_7 = 9.61 \times 10^7$	$\tau_7 = 789$	$G_7 = 1.30 \times 10^7$	$\tau_7 = 827$

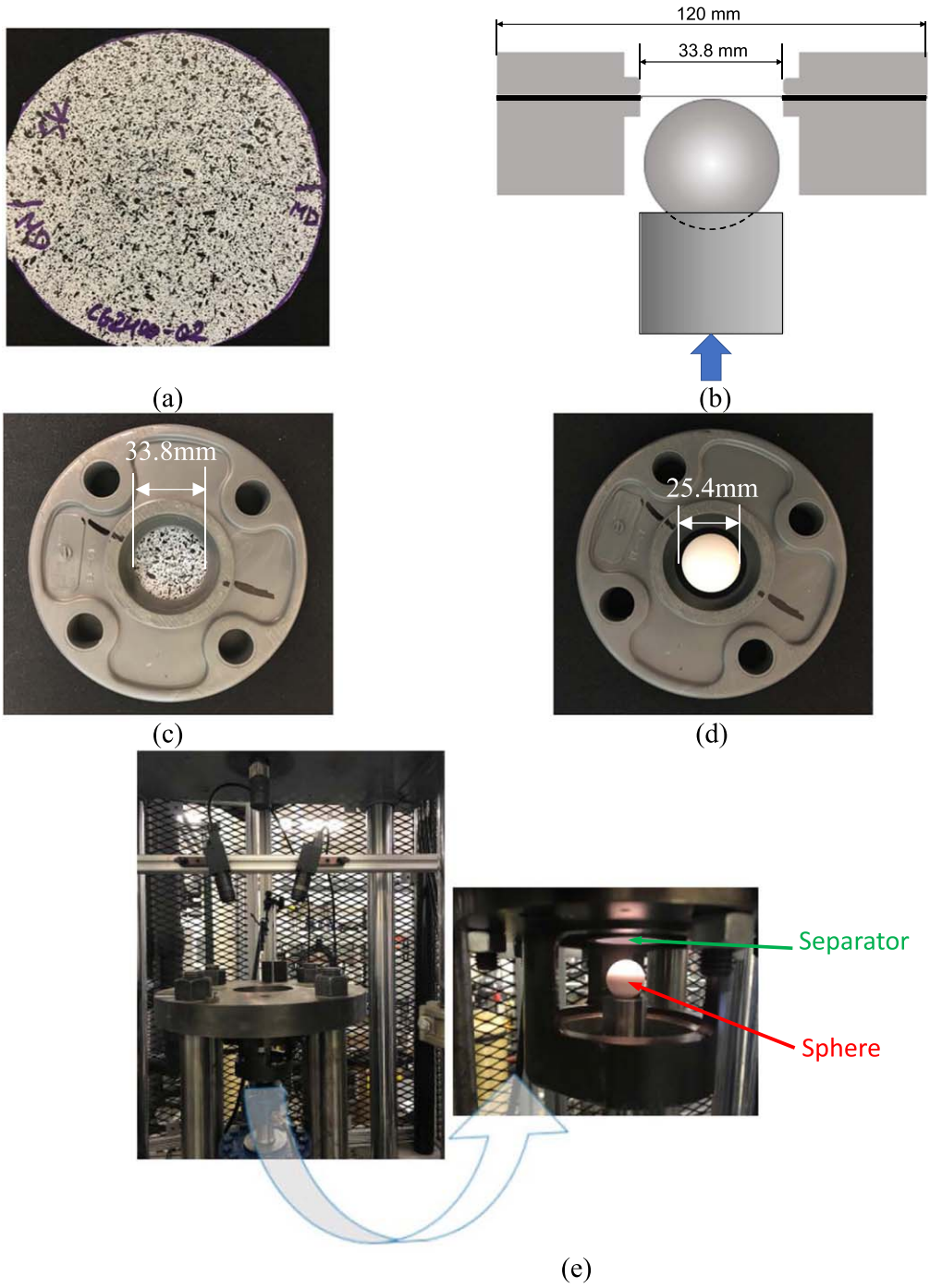

Figure 3. The experimental set-up for punch test. (a) a Celgard® 2400 circular sample of diameter 120 mm with sprayed speckles. (b) Schematic plot of a sample sandwiched in a flange. (c) The flange with a separator sample. (d) The flange and Polytetrafluoroethylene (PTFE) sphere. (e) The load is applied with a PTFE solid sphere.

Lagrangian strains were calculated using neighboring points and Gaussian smoothing were applied with the center at the current point of interest. From these values, the principal strains (or other variables of interest) were calculated.

Results and Discussion: Material Model Verification and Validation

The orthotropic viscoelastic model has been implemented in LS-DYNA as a user material model for shell element. The model was verified using one element test under various creep loading conditions, and validated against tensile test at different rate. The model was also validated under biaxial loading by simulating the punch test.

Model verification.—The implemented orthotropic viscoelastic model was verified with one element test. To complete the simulations using LS-DYNA explicit solver within a reasonable time period, the input relaxation modulus was scaled up by three decades such that a simulation time of 1 ms will correspond to 1 s in real time. This practice was used in all simulations reported in the current paper.

Table II. Analytical solutions.

Uniaxial Loading	Analytical solution
Stress relaxation[13]	$\sigma(t) = \Delta\varepsilon_{y0} \times G(t)$
Creep test[13]	$\varepsilon(t) = \Delta\sigma_{y0} \times J(t)$
Creep test with two steps (case 1)[13]	• $0 \sim 2$ s, $\varepsilon(t) = \Delta\sigma_1 \times J(t) = 1 \times J(t)$ • $2 \sim 4$ s, $\varepsilon(t) = \Delta\sigma_1 \times J(t) + \Delta\sigma_2 \times J(t-2) = 1 \times J(t) + 1 \times J(t-2)$
Creep test with two steps (case 2)[13]	• $0 \sim 2$ s, $\varepsilon(t) = \Delta\sigma_1 \times J(t) = 2 \times J(t)$ • $2 \sim 4$ s, $\varepsilon(t) = \Delta\sigma_1 \times J(t) + \Delta\sigma_2 \times J(t-2) = 2 \times J(t) - 1 \times J(t-2)$

Comparison with MAT76.—LS-DYNA has a general viscoelastic material model MAT76.[19] MAT76 is for isotropic linear viscoelastic material. The implemented model was compared with MAT76 for a fictional isotropic material with the Celgard® 2400 MD relaxation modulus reported in Ref. 4. The one element test was performed for four sets of uniaxial loading conditions: stress relaxation, creep, and creep test with two steps for two cases: low-high and high-low.

The material responses for these loading conditions were also computed using analytical solution following,[13,20] as listed in Table II. In Table II, *J(t)* is the creep compliance. Prony series parameters for the creep compliance of Celgard® 2400 have been determined in the previous work.[4]

Figures 4a–4d present comparisons of the simulation results using MAT76, user material model and the analytical solutions for stress relaxation, creep and creep with two-step loadings. The results obtained using these three methods agreed well for the four tested loading conditions. This indicates that the algorithm for the evaluation of hereditary integral with a kernel of Prony series presented in section 2.1 was implemented correctly.

Verification with creep experiments.—In a previous work,[15] Celgard® 2400 has been tested along the MD, TD, and 45° off-axis directions under creep loadings. DIC was used for strain measurement in these experiments. These are good verification cases for the current model.

Figure 5 compares the creep strains obtained by experiments and by one element simulation using user material model. The experimental curve is the averaged curve from 2–4 measurements. Figures 5a and 5b present the longitudinal creep strain for tests performed with samples cut along the MD and TD directions, respectively. Figure 5c presents the longitudinal strain for samples cut in 45° off-axis direction. The predicted creep strains agree well with the experimental data for all cases.

Validation with tensile test.—In the previous work,[15] tensile tests were performed for samples cut along the MD, TD and 45° off-axis directions at loading rates of 0.1 N min^{-1}, 1 N min^{-1}, and 10 N min^{-1}. These experiments were simulated with one element test. Figure 6 compares the predicted stress-strain curves with the

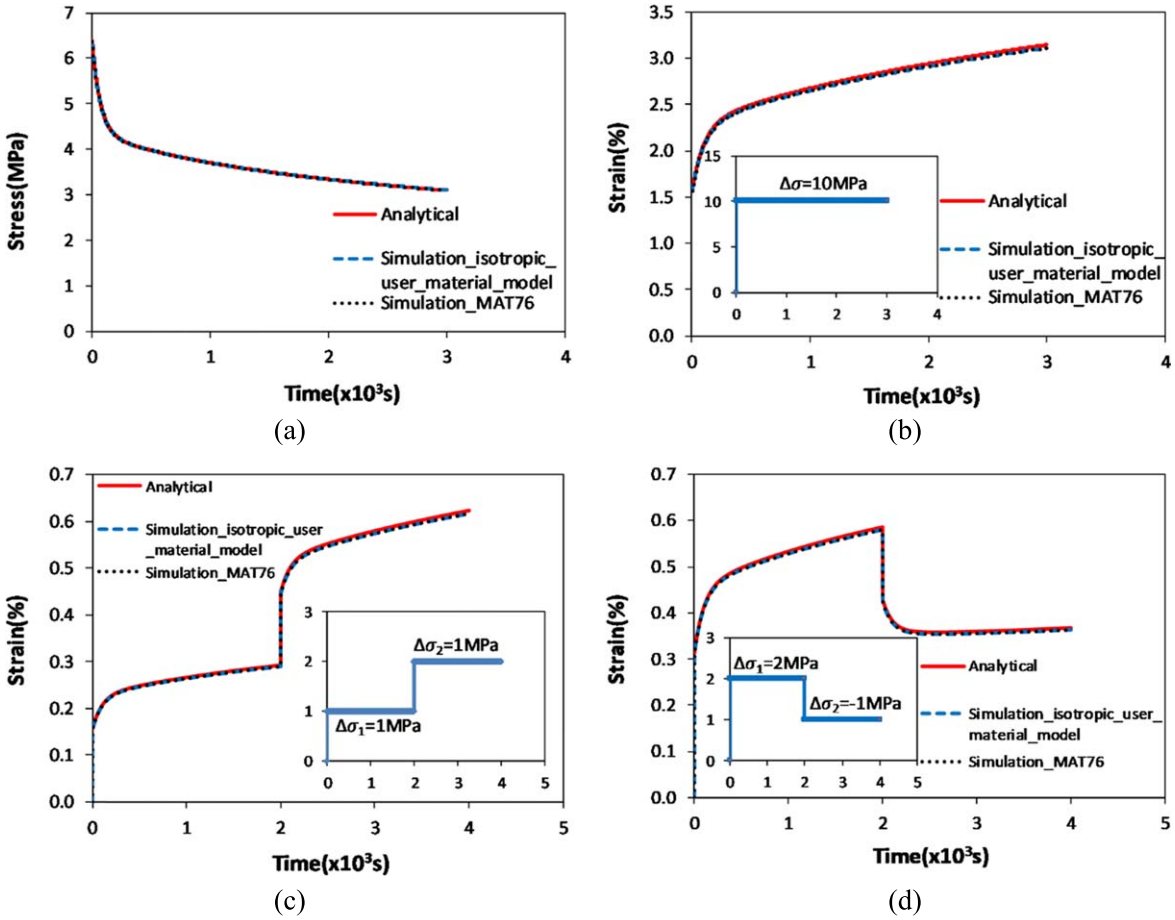

Figure 4. Comparison of predicted strain histories using one element test with MAT76, user material model, and analytical solutions for uniaxial loading under (a) stress relaxation, (b) creep, and creep test with two steps: (c) low-high, and (d) high-low.

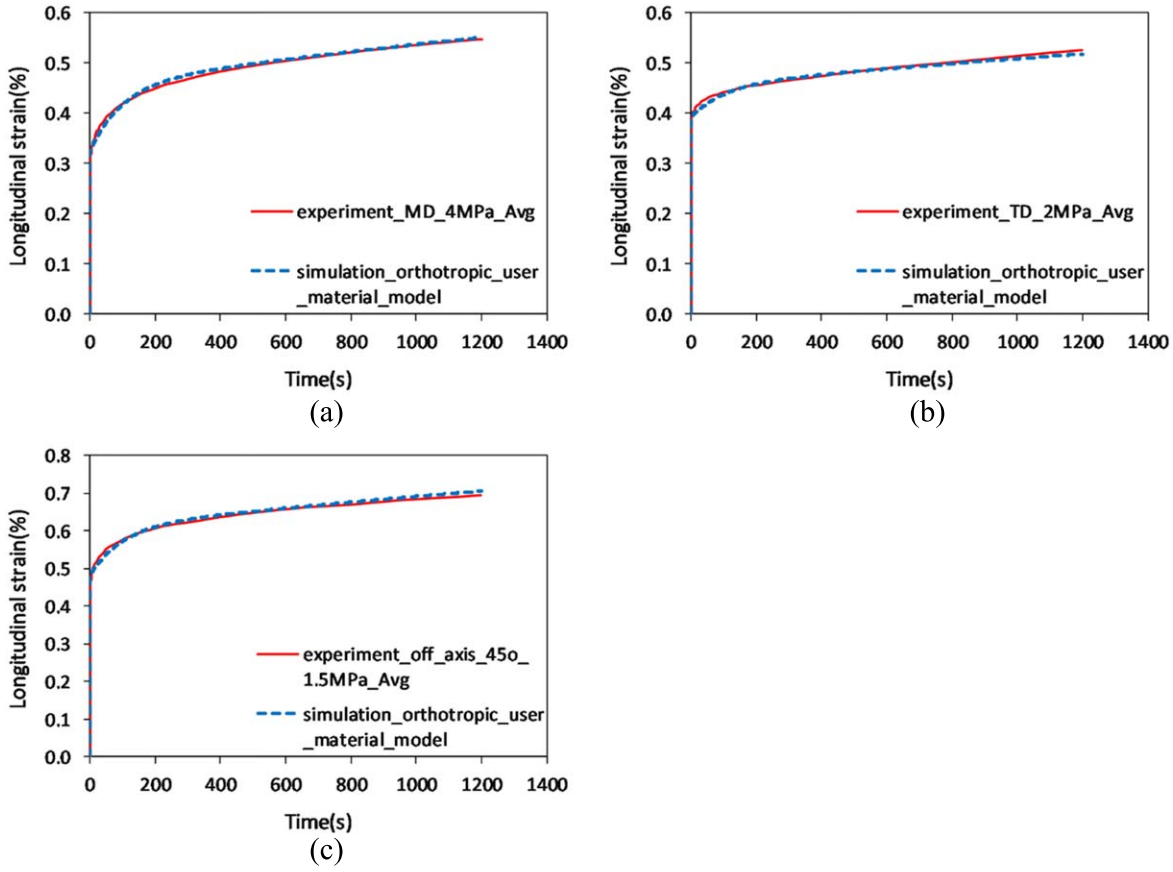

Figure 5. Comparison of one element simulation with experimental data for samples being subjected to uniaxial creep (a) along the MD, (b) along the TD, and (c) 45° off-axis direction.

experimental curves. There was some scatter in experimental data and hence two representative curves were presented for each loading condition. As seen in Fig. 6, the simulations captured the trend of rate dependence in all three directions. With increasing the loading rate, the material behaved stiffer with a higher modulus.

Experimental curves in the MD and TD displayed a gradual stiffening behavior at small strain region. This is particularly noticeable in Fig. 6a, i.e. in the MD. It should be noted that this response is not intrinsic to the material but caused by difficulties in specimen mounting in experiment. Besides the small strain regions, the predicted MD and TD stress-strain curves agreed with the experimental curves reasonably well. Figure 6c presents the stress-strain curves for 45° off-axis tensile in the longitudinal direction. The predicted stress-train curves were softer than the experimental curves. Table III compares the predicted and measured modulus at the three rates. The predicted longitudinal modulus for 45° off-axis tensile was about 6%–11% lower than the experimental values.

In summary, simulations using the user material model with the linear orthotropic viscoelastic properties established in a previous work[15] provided reasonable predictions for the rate dependent stress-strain behaviors in the MD, TD, and 45° off-axis direction. The results show that the rate dependent behavior of the separator can be captured in FE simulations by using an orthotropic viscoelastic constitutive model.

Validation with biaxial punch tests.—The user material model was examined under biaxial loading by simulating the punch test. Figure 7 presents the FE model used for this simulation. Here, only the separator and the punch were modeled explicitly. The boundary condition of the flange-rubber-separator assembly was modeled by constraining the nodes under the flanges. The flange has an inner opening of 33.8 mm diameter. However, fully constraining the nodes at this distance resulted in a much stiffer response than the experiment. It was realized that the area of the sample beyond the inner opening is not necessarily fully constrained in all six degrees of freedom. The full constraint would be achieved at a radial distance larger than the inner opening, i.e. $R > 16.9$ mm. In this work, it was assumed that a full constraint was

Table III. Comparison of predicted and measured tensile moduli[a].[15]

	MD modulus (MPa)			TD modulus (MPa)			45° longitudinal modulus (MPa)		
Force ramp rate (N/min)	Exp.	Sim.	Error (%)	Exp.	Sim.	Error (%)	Exp.	Sim.	Error (%)
0.1	955 ± 31	863	−9.6	485 ± 17	453	−6.6	290 ± 10	271	−6.6
1	1134 ± 23	1107	−2.4	510 ± 18	500	−2.0	323 ± 27	305	−5.6
10	1282 ± 9	1216	−5.1	526 ± 1	510	−3.0	351 ± 6	312	−11.1

a) in the range of 0.1%–0.5% strain.

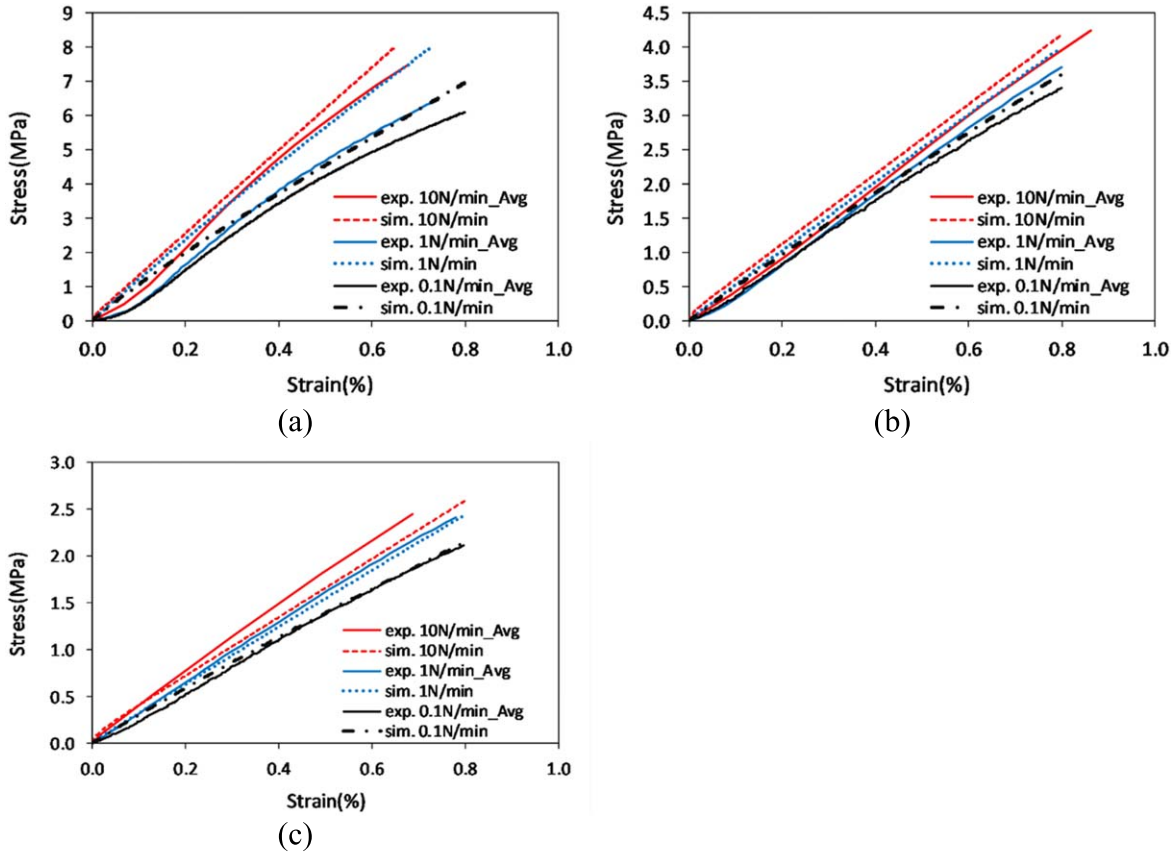

Figure 6. Comparison of simulated stress-strain responses with experimental data at different force ramp rates[15] for tensile test with sample cut (a) along the MD, (b) along the TD, and (c) along the 45° off-axis direction.

achieved about the halfway of the flange width, i.e. at a radial distance R = 40 mm. The nodes under the flanges but with a radial distance less than 40 mm were constrained in the z-direction only, as illustrated in Fig. 7.

The punch was modeled as a semi-sphere. It was prescribed with a constant velocity of 0.2 mm ms^{-1} in the z direction in simulations. As mentioned in section 4.1, with a relaxation modulus increased by three decades, 1 ms simulation is equivalent to 1 s in real time. Therefore, the ball is moving at the same speed as in experiment. The contact between the punch and the sample was defined with a static friction coefficient of 0.4 and a dynamic friction coefficient of 0.2.

Figure 8 compares the strain fields at the sample surface measured using the DIC technique and the FE predictions. The

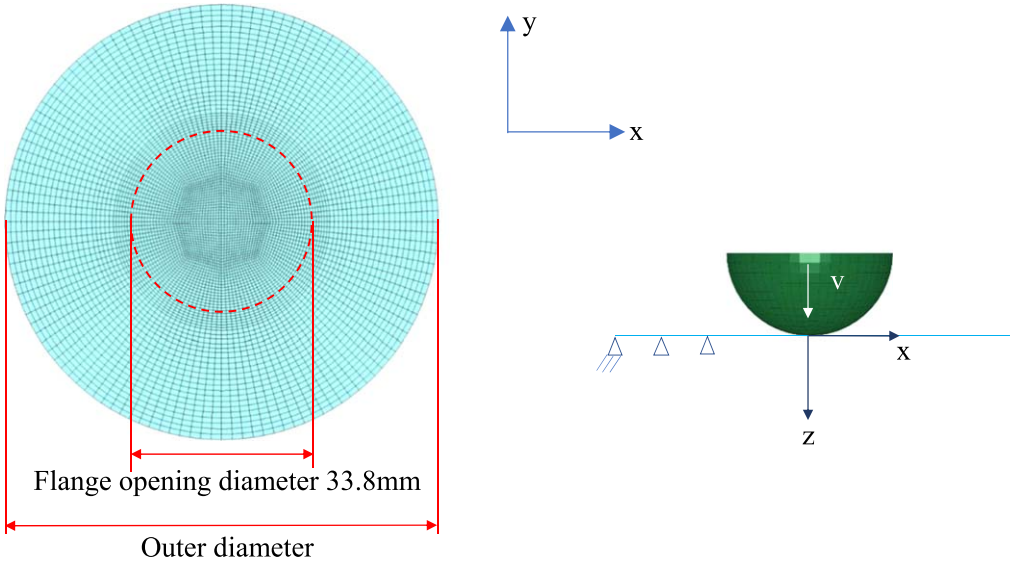

Figure 7. The FE model for biaxial punch experiment includes the specimen and the punch. For the specimen, the nodes at a radial distance 16.9 mm < R < 40 mm were constrained in z-direction only. The nodes at R = 40 mm were fully constrained.

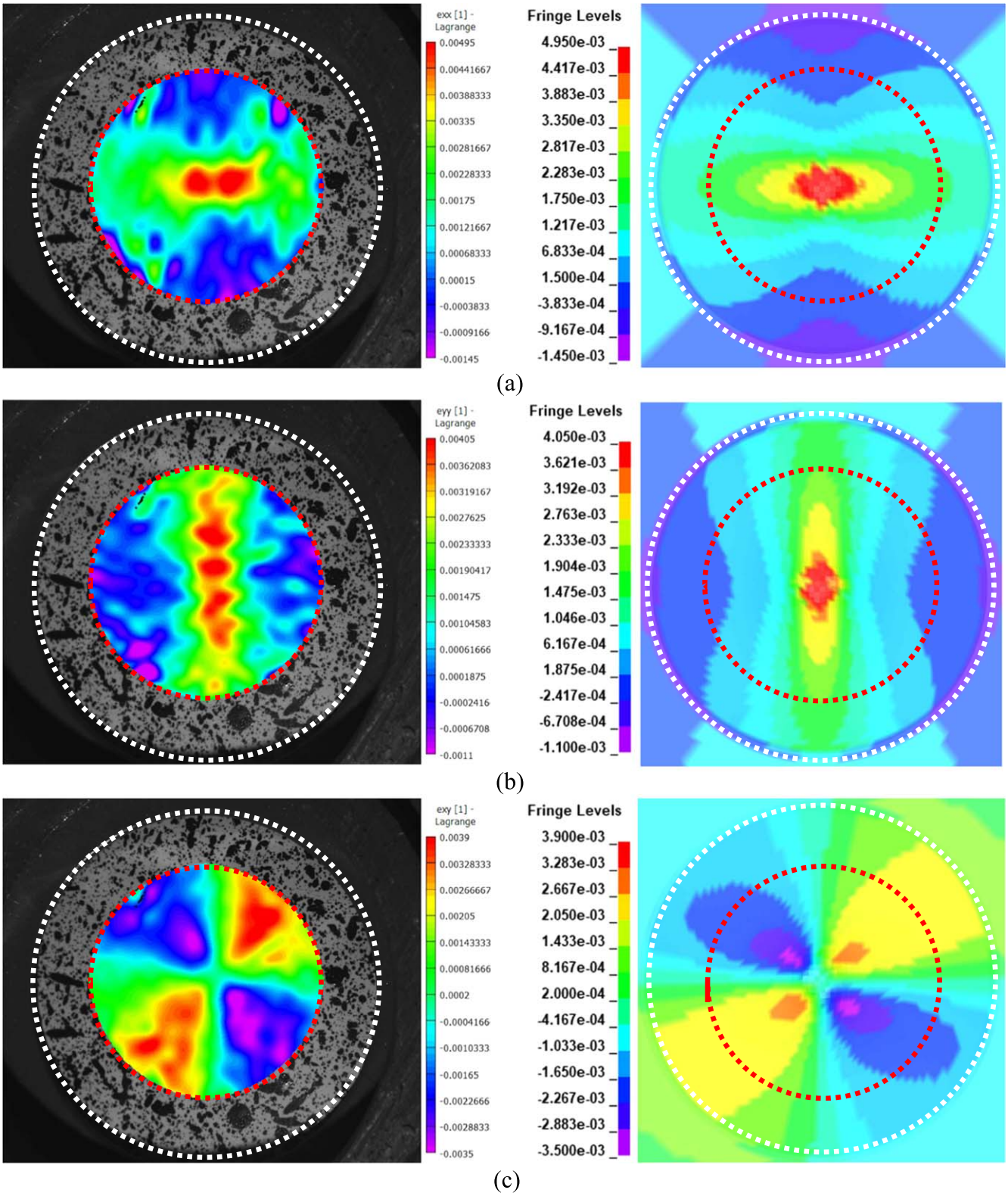

Figure 8. Strain contours at the upper surface of the sample in punch test, (left) measured using DIC technique, (right) predicted using the user material model. (a) The TD strain with a maximum of 0.5%, and the corresponding (b) MD strain, (c) tensorial shear strain, (d) the 1st principal strain, and (e) the 2nd principal strain. The white dotted circle represents flange opening with diameter 33.8 mm while the red dotted circle represents the area analyzed in Vic3D.

images in the left column are the DIC results and at the right are the predictions. The comparison was made at the instant when the maximum strain in TD (e_{xx}) reaches 0.5%. Figures 8a–8e present the TD strain (e_{xx}), MD strain(e_{yy}), tensorial shear strain (e_{xy}), 1st principal strain, and 2nd principal strain, respectively. The tensorial shear strain is one half of the engineering strain. To facilitate the comparison, the strain range of the FE results was defined the same as the DIC results. As shown, the predicted strain patterns agreed

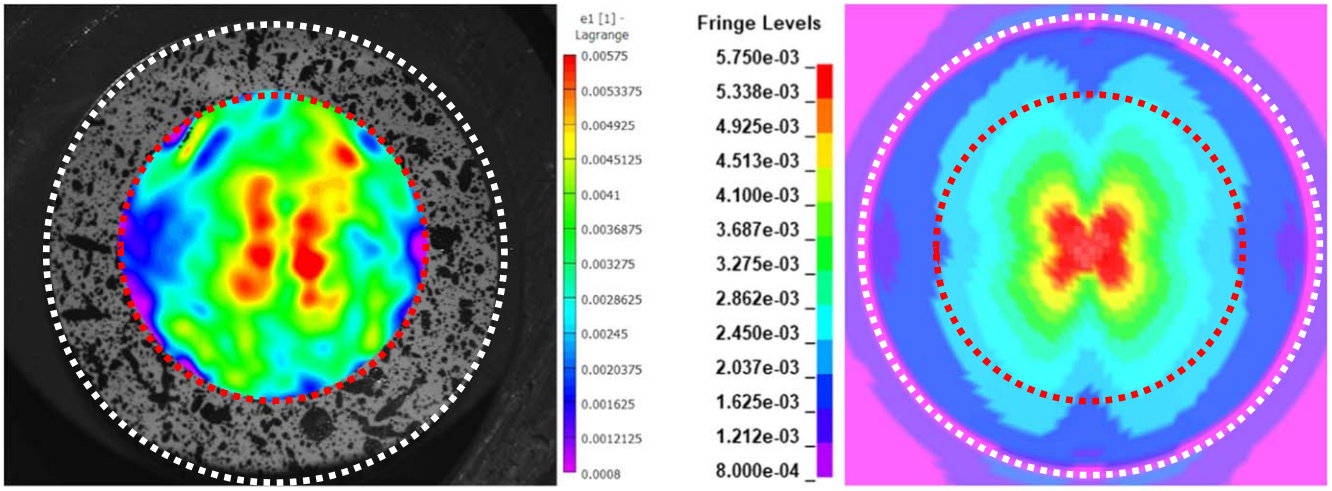

(d)

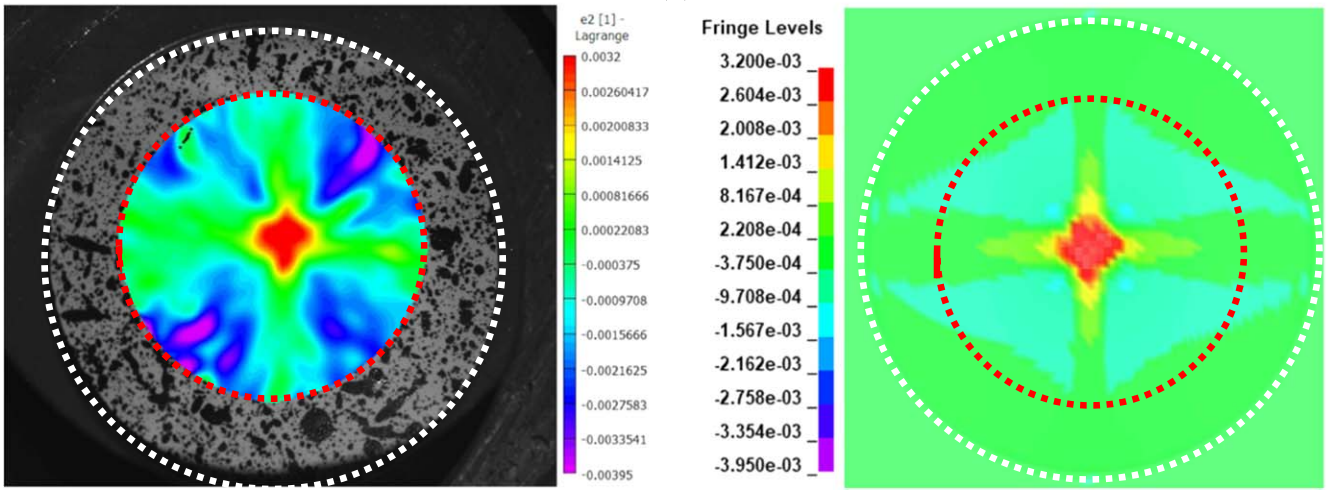

(e)

Figure 8. Continued.

well with experimental results for every strain components. Figures 8a and 8b show that, when the maximum TD strain was at 0.5%, the MD strain was smaller with a maximum value of 0.405%. Furthermore, the MD strain contours were more elongated than the TD contours. The same trend is observed in DIC results and in simulations. Figure 8c compares the shear strain. The predicted shear strain pattern agreed with the DIC results well. However, the predicted value was slightly lower. Figures 8d and 8e compare the 1st and 2nd principal strain fields. The orthotropic model predicted a butterfly like contour for the 1st principal strain and a cross like shape for the 2nd principal strain. These predictions matched with DIC results in terms of the contour pattern and the magnitude.

To demonstrate the difference between the orthotropic and isotropic viscoelastic models, the punch test simulation was also performed using MAT76 with the MD viscoelastic property. Figure 9 presents the predictions using MAT76 at the instant when the TD strain is 0.5%. With an isotropic model, the obtained strain contours (in supplementary material) were very different from the DIC results. The strain contours and the magnitude for the MD were exactly the same as that of TD at 90° rotation. The two principal strain contours have a circular shape. In conclusion, the prediction by using the user material model matches the DIC results much better than that of using MAT76.

The current model establishes the foundation for modeling the orthortropic viscoelastic behavior of the separator. In the next step, the model will be extended to include the temperature dependent and nonlinear behavior. The model will also consider the effect of the electrolyte on the viscoelastic behavior of the polymer separators.[4–8,21,22] This model will improve the prediction of the mechanical integrity of the separator in batteries in coupled thermal-mechanical simulations.

Conclusions

A linear orthotropic viscoelastic model has been developed and implemented as a user material model in the commercial FE package LS-DYNA®, where a discretization algorithm for the evaluation of a stiffness-based hereditary integral has been extended to a kernel of Prony series from a single exponential function. The developed model was applied to Celgard® 2400, a monolayer PP separator. The simulation results were verified and validated with experimental data under a variety of loading conditions, including uniaxial tensile creep, uniaxial tensile experiments along different directions at different rate, and biaxial tension. The model prediction of anisotropy and rate dependence of the separator agrees well with experimental data.

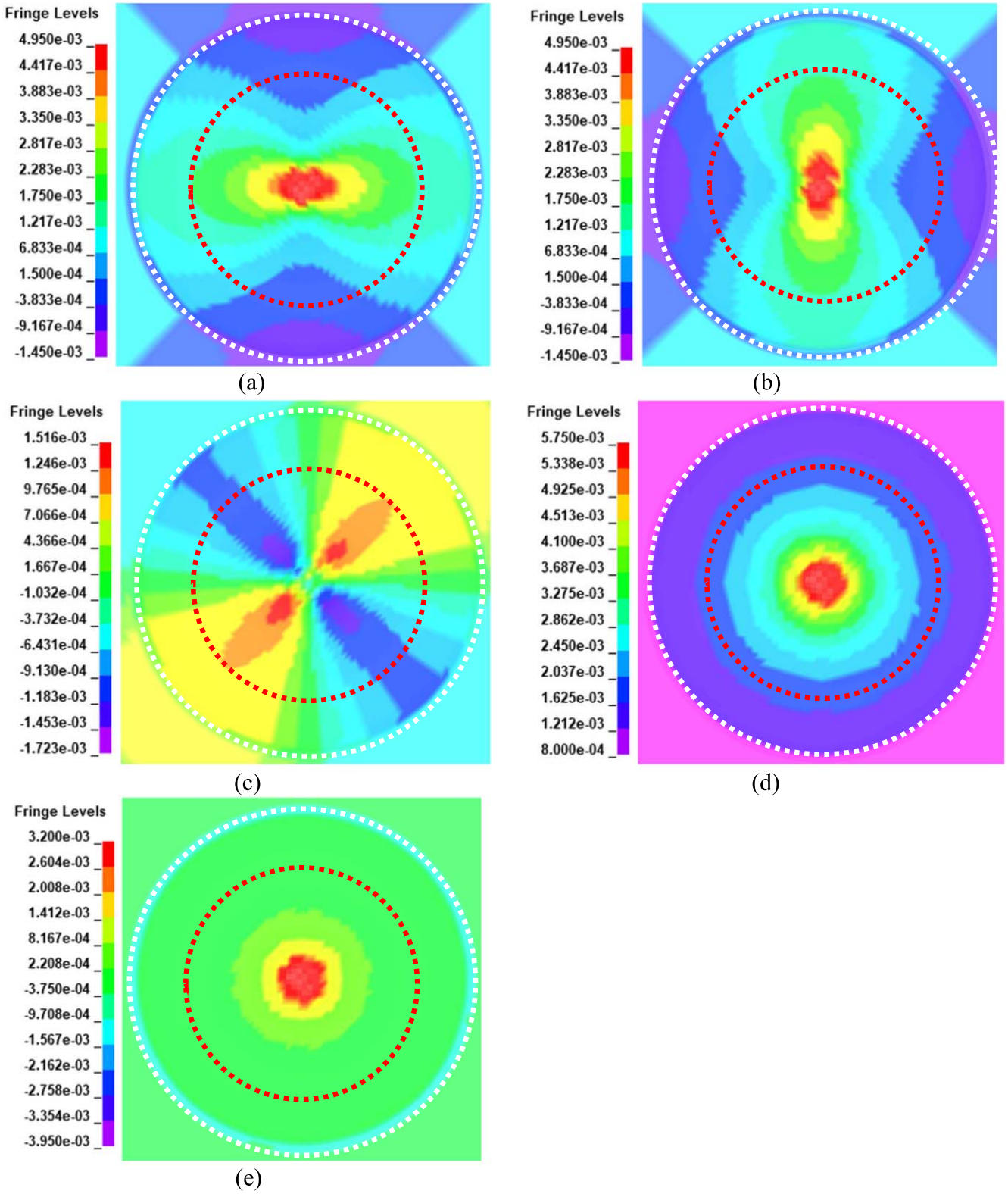

Figure 9. Strain fields in punch test predicted with an isotropic viscoelastic model. (a) The TD strain with a maximum of 0.5%, and the corresponding (b) MD strain, (c) shear strain (in tensor), (d) the 1st principal strain, and (e) the 2nd principal strain.

Acknowledgments

This work is supported by the Ford-University Alliance Program. Research at Oak Ridge National Laboratory, managed by UT-Battelle, LLC, for the U.S. Department of Energy under contract DE-AC05-00OR22725, was sponsored by the by the Vehicle Technologies Program for the Office of Energy Efficiency and Renewable Energy. Notice: This manuscript has been authored by UT-Battelle, LLC under Contract No. DE-AC05-00OR22725 with the U.S. Department of Energy. The United States Government retains and the publisher, by accepting the article for publication,

acknowledges that the United States Government retains a non-exclusive, paid-up, irrevocable, world-wide license to publish or reproduce the published form of this manuscript, or allow others to do so, for United States Government purposes. The Department of Energy will provide public access to these results of federally sponsored research in accordance with the DOE Public Access Plan (http://energy.gov/downloads/doe-public-access-plan).

ORCID

Jie Deng https://orcid.org/0000-0001-9883-7770
Xinran Xiao https://orcid.org/0000-0003-4459-5774

References

1. P. Arora and Z. Zhang, *Chem. Rev.*, **104**, 4419 (2004).
2. S. Yan, J. Deng, C. Bae, and X. Xiao, *Polym. Test.*, **71**, 65 (2018).
3. J. Zhu, T. Wierzbicki, and W. Li, *J. Power Sources*, **378**, 153 (2018).
4. A. Sheidaei, X. Xiao, X. Huang, and J. Hitt, *J. Power Sources*, **196**, 8728 (2011).
5. J. Xu, L. Wang, J. Guan, and S. Yin, *Mater. Design*, **95**, 319 (2016).
6. I. Avdeev, M. Martinsen, and A. Francis, *J. Mater. Eng. Perform.*, **23**, 315 (2014).
7. J. Cannarella, X. Liu, C. Z. Leng, P. D. Sinko, G. Y. Gor, and C. B. Arnold, *J. Electrochem. Soc.*, **161**, F3117 (2014).
8. G. Y. Gor, J. Cannarella, J. H. Prévost, and C. B. Arnold, *J. Electrochem. Soc.*, **161**, F3065 (2014).
9. W. Wu, X. Xiao, X. Huang, and S. Yan, *Comput. Mater. Sci.*, **83**, 127 (2014).
10. R. Behrou, *ECS Trans.*, **80**, 583 (2017).
11. X. Zhang, E. Sahraei, and K. Wang, *J. Power Sources*, **327**, 693 (2016).
12. M. Martinsen, "Material behavior characterization of a thin film polymer used in lithium-ion batteries." *Master's Thesis*, The University of Wisconsin-Milwaukee (2012), https://dc.uwm.edu/etd/36.
13. J. D. Ferry, *Viscoelastic Properties of Polymers* (Wiley, New York) (1980).
14. I. M. Ward and J. Sweeney, *An Introduction to the Mechanical Properties of Solid Polymers* (Wiley, New York) (2004).
15. S. Yan, J. Deng, C. Bae, Y. He, A. Asta, and X. Xiao, *Polym. Test.*, **72**, 46 (2018).
16. M. A. Puso and J. A. Weiss, *J. Biomech. Eng.*, **120**, 62 (1998).
17. J. Li, K. Kwok, and S. Pellegrino, *Mech. Time-Depend. Mater.*, **20**, 13 (2016).
18. S. Kalnaus, A. Kumar, Y. Wang, J. Li, S. Simunovic, J. A. Turner, and P. Gorney, *J. Power Sources*, **378**, 139 (2018).
19. LSTC, *LS-DYNA® Keyword User's Manual*, Livermore Software Technology Corporation, Livermore, CA (2017), https://dynasupport.com/manuals/ls-dyna-manuals/ls-dyna-manual-r-9.0-vol-ii/view.
20. I. M. Daniel and O. Ishai, *Engineering Mechanics of Composite Materials* (Oxford University Press, Oxford) (2006).
21. G. Y. Gor, J. Cannarella, C. Z. Leng, A. Vishnyakov, and C. B. Arnold, *J. Power Sources*, **294**, 167 (2015).
22. J. Chen, H. Hu, S. Li, and Y. He, *J. Appl. Polym. Sci.*, **135**, 46441 (2018).